Journal of Applied Physics

RESEARCH ARTICLE | DECEMBER 18 2025

Modeling strain and quantum confinement in GaAs/$Ga_xIn_{1-x}P$ superlattices for spin-polarized electron sources

A. Kachwala ✉ ; G. Blume ; S. Marsillac ; J. Grames ; M. Grau

J. Appl. Phys. 138, 234902 (2025)
https://doi.org/10.1063/5.0300193

AIP Publishing

Journal of Applied Physics ARTICLE pubs.aip.org/aip/jap

Modeling strain and quantum confinement in GaAs/$Ga_xIn_{1-x}P$ superlattices for spin-polarized electron sources

Cite as: J. Appl. Phys. **138**, 234902 (2025); doi: 10.1063/5.0300193
Submitted: 31 August 2025 · Accepted: 2 December 2025 ·
Published Online: 18 December 2025

A. Kachwala,[1,a)] G. Blume,[2] S. Marsillac,[3] J. Grames,[1] and M. Grau[2]

AFFILIATIONS

[1]Center for Injector and Sources, Thomas Jefferson National Accelerator Facility, 12000 Jefferson Avenue, Newport News, Virginia 23606, USA
[2]Department of Physics, Old Dominion University, 5115 Hampton Blvd, Norfolk, Virginia 23529, USA
[3]Department of Electrical and Computer Engineering, Old Dominion University, 5115 Hampton Blvd, Norfolk, Virginia 23529, USA

[a)]**Author to whom correspondence should be addressed:** kachwala@jlab.org

ABSTRACT

In this study, we systematically design and simulate a series of GaAs-based superlattice configurations aimed at enhancing heavy-hole–light-hole band splitting while simultaneously optimizing band alignment to reduce the conduction band barrier, thereby facilitating efficient electron transport. These combined effects are crucial for achieving high electron spin polarization and high quantum efficiency, the two key performance metrics of next-generation spin-polarized electron sources. We investigated three types of superlattice architectures: (1) compressively strained GaAs wells on GaInP barriers, yielding a maximum band splitting of 140 meV, (2) lattice-matched GaAs/GaInP structures, resulting in the maximum band splitting of 75 meV, and (3) tensile strained GaAs wells on GaInP barriers, with a maximum band splitting of 40 meV. The results demonstrate the tunability of heavy-hole–light-hole band splitting and establish a design framework for high-performance spin-polarized photocathodes based on a combination of strain engineering, quantum confinement, and optimized heterostructure design.

I. INTRODUCTION

Spin-polarized electron sources have found widespread applications across various fields, particularly in accelerator-based research.[1] These sources have been integral components at several accelerator facilities, including the Stanford Linear Accelerator Center (SLAC),[2–4] Mainz Microtron (MAMI),[5] and the Continuous Electron Beam Accelerator Facility (CEBAF) at Jefferson Lab.[6] In the context of high-energy and nuclear physics, spin-polarized electron beams have enabled a number of high-impact experiments, such as precision measurements of the strangeness content in the nucleon,[7] stringent tests of the Standard Model,[8] and determinations of the neutron radius in heavy nuclei such as ^{208}Pb.[9]

Looking ahead, spin-polarized electron sources are expected to play an even more critical role in the MOLLER experiment[10] and future experiments at next-generation facilities such as the Electron-Ion Collider (EIC).[11] These experiments demand stringent beam parameters, including electron spin polarization (ESP) of at least 85% and luminosities as high as $10^{34}\,cm^{-2}\,s^{-1}$.[12] To meet these challenges, polarized electron sources must offer not only high ESP but also high quantum efficiency (QE) to maximize the product $ESP^2 \cdot QE$, a commonly used figure of merit for evaluating the performance of such sources.[13,14] Furthermore, for parity-violation experiments, even a modest QE anisotropy—where the photoemission yield depends on the polarization or orientation of the incident light[15]—of the order of 4%–5% can introduce significant systematic errors. Therefore, reducing the QE anisotropy further could have a significant impact on the experimental accuracy.[10]

The underlying mechanism for spin-polarized photoemission from photocathodes relies on three key mechanisms: (1) optical

absorption using circularly polarized photons to selectively excite electrons, (2) transport of excited electrons to the photocathode-vacuum interface, and (3) efficient emission of these electrons into the vacuum via a negative electron affinity (NEA) surface. For several decades, gallium arsenide (GaAs) is the only practical material used for high-polarization spin-polarized electron sources. As a direct bandgap semiconductor, bulk GaAs features degenerate heavy-hole (HH) and light-hole (LH) valence bands at the Brillouin zone center (the Γ point). However, due to the degeneracy and mixing of HH and LH states during optical excitation, the theoretical maximum ESP from bulk GaAs is limited to approximately 50%.[16–18]

To surpass this limit, modern photocathode designs employ strained-layer structures where GaAs is deposited on a lattice-mismatched wider bandgap III–V semiconductor. The in-plane strain experienced by GaAs can be either tensile or compressive, depending on the lattice constant of the underlying substrate. Compressive strain arises when the substrate has a smaller lattice constant than GaAs, forcing the GaAs layer to compress laterally. Conversely, tensile strain occurs when the substrate has a larger lattice constant, stretching the GaAs layer in-plane. In compressively strained GaAs photocathodes, such as those grown on gallium arsenide phosphide (GaAsP) substrates, the lattice mismatch introduces strain in the GaAs that lifts the degeneracy between the HH and LH bands, leading to valence band splitting, defined as the energy difference between the light-hole and heavy-hole bandgaps, with HH having a smaller bandgap as compared to LH. This strain-induced splitting allows selective excitation of only the HH band in the GaAs well, reducing LH excitation contamination and theoretically allowing ESP values of 100% with experimental values reported to be around 80% with QE around 0.1%.[19,20]

Even greater control over spin polarization is achieved using superlattice structures.[20,21] These multi-quantum well designs consist of alternating layers of GaAs as the quantum well and a wider-bandgap barrier material, which serve to enhance the separation between HH and LH valence bands through a combination of strain and quantum confinement effects.[22] The resulting periodic potential can further increase the HH–LH splitting, thereby leading to high ESP and QE during photoexcitation.[23] The superlattice structure further preserves the built-in strain and thus the ESP over a larger volume, unlike a single thick GaAs layer where the strain tends to relax beyond a critical thickness as described by the Matthews–Blakeslee model.[24]

For example, in a GaAs/$GaAs_{0.65}P_{0.35}$ superlattice structure with 1% compressive strain applied to the GaAs wells, the HH–LH energy splitting can reach approximately 80 meV, due to strain and quantum confinement.[25,26] However, this material system typically exhibits an unfavorable band alignment: nearly 60% of the bandgap difference between GaAs and $GaAs_{0.65}P_{0.35}$ contributes to the conduction band offset (CBO), leaving a smaller portion for the valence band offset (VBO). This configuration with a smaller VBO results in reduced splitting between HH and LH bands due to quantum confinement effects. In addition, the larger CBO can also impede efficient conduction band electron transport, reducing overall quantum efficiency despite relatively higher spin polarization. Furthermore, the compressive strain used to achieve the desired band splitting can introduce crystal defects in the superlattice structure. These defects, intersecting with the electron transport path, can act as spin-flip scattering centers, leading to additional spin depolarization and further lowering the maximum achievable ESP.[27,28]

In contrast, a GaAs/$Al_{0.35}Ga_{0.65}As$ superlattice typically experiences 0.2% tensile strain on the GaAs layers, leading to an HH–LH splitting of approximately 40 meV, primarily driven by quantum confinement.[23] Furthermore, the defects introduced in the crystal due to tensile strain are located parallel to the electron transport path and have negligible effect on the ESP.[28] However, the CBO at the GaAs/$Al_{0.35}Ga_{0.65}As$ interface is relatively large, of the order of 300 meV. This offset accounts for approximately 65% of the total bandgap difference between the two materials. Furthermore, the interface exhibits a higher conduction band mass discontinuity factor, defined as the ratio of the conduction band effective mass in the barrier to that in the well. This increased discontinuity along with larger CBO impedes the transport of electrons in the conduction band across the superlattice structure.[23,29–31]

To enable efficient spin-polarized electron emission at room temperature, a total HH-LH splitting of 40 meV or greater is generally considered necessary, as it suppresses thermal population of the LH band and ensures high polarization.[32] Moreover, to enhance quantum confinement effects along with promoting efficient electron transport across the superlattice, it is critical that the majority of the bandgap difference between the well and barrier materials be associated to the VBO, with only a minimal portion relating to the CBO. This band alignment strategy maximizes hole confinement without impeding conduction band electron transport, optimizing both polarization and quantum efficiency. In addition, a minimized conduction band mass discontinuity factor can further lead to improved electron tunneling across the superlattice photocathode.[31] Furthermore, in strained superlattice structures, it is desirable to have tensile strain over compressive strain as it can potentially lead to fewer defect-induced spin-flip scattering events, thereby enabling the achievement of higher ESP.

In this work, we investigate various combinations of well and barrier materials to achieve HH–LH band splitting exceeding 40 meV by engineering splitting due to strain as well as quantum confinement. We selected GaAs as the well material due to its direct bandgap, favorable optical properties, and mature epitaxial growth technology. We chose the barrier material based on three key criteria: (1) a favorable band alignment with GaAs that ensures strong hole confinement, enhancing splitting through quantum confinement without impeding conduction band electron transport; (2) a minimized conduction band mass discontinuity factor—defined as the ratio of the conduction band effective mass in the barrier to that in the well—to improve electron tunneling across the superlattice;[31] and (3) a ternary alloy composition with a bandgap larger than GaAs to facilitate epitaxial growth and avoid the fabrication complexities associated with quaternary or higher-order alloys. Based on these considerations, we identified gallium indium phosphide (GaInP) as an optimal barrier material. In this study, we designed and simulated three distinct superlattice configurations: (1) 1% compressively strained GaAs wells on GaInP barriers, (2) lattice-matched GaAs/GaInP superlattices, and (3) 1% tensile strained GaAs wells on GaInP barriers. For the case of compressive

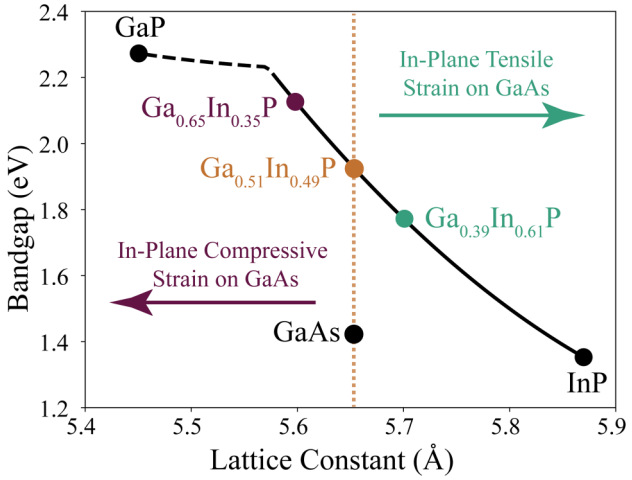

FIG. 1. The lattice constants and bandgap energies for GaAs well and the corresponding barrier materials. The orange dashed line indicates the lattice constant of GaAs, serving as a reference for lattice-matched conditions. The solid black line represents the direct bandgap, and the dashed black line represents the indirect bandgap of $Ga_xIn_{1-x}P$ barrier materials.[30]

strain, increasing the Ga fraction (x) in $Ga_xIn_{1-x}P$ barriers beyond $x = 0.65$ enhances heavy-hole/light-hole splitting due to both increased strain and stronger quantum confinement resulting from a larger VBO. However, for $x > 0.70$, $Ga_xIn_{1-x}P$ becomes an indirect bandgap material, leading to significantly longer tunneling lifetimes[33,34] that can reduce the quantum efficiency of the superlattice photocathode. Therefore, in our simulations, we limited our analysis to structures with 1% compressive strain, and for comparison, also considered structures with 1% tensile strain. Figure 1 summarizes the relevant lattice constants and bandgap energies of GaAs and the corresponding barrier compositions explored in this work.

II. MODELING APPROACH AND MATERIAL PARAMETERS

Strain-induced modifications to the band structure of crystalline semiconductors have been extensively investigated, both theoretically and experimentally.[35] When a sufficiently thin epitaxial layer of GaAs is grown on a barrier material with a different lattice constant, it experiences biaxial compressive or tensile strain in the plane of the interface, depending on the lattice mismatch. Full pseudomorphic strain is achieved when the GaAs layer adapts to the in-plane lattice constant of the barrier without introducing significant dislocations.

This strain alters the band structure of GaAs, resulting in both a shift and splitting of the valence band states. To calculate the strain-dependent band edge energies of the HH and the LH bands with respect to the conduction bands in GaAs, we employed the following expressions:[36]

$$E^{C}_{HH} = E_g(\mathrm{GaAs}) + \Delta E_H - \Delta E_S, \tag{1}$$

$$E^{C}_{LH} = E_g(\mathrm{GaAs}) + \Delta E_H + \Delta E_S - \frac{(\Delta E_S)^2}{\Delta_0}. \tag{2}$$

Here, $E_g(\mathrm{GaAs})$ denotes the bandgap of fully relaxed GaAs and Δ_0 is the spin–orbit splitting energy. The terms ΔE_H and ΔE_S represent the hydrostatic shift of the center of gravity of the $P_{3/2}$ valence multiplet and the linear splitting of that multiplet, respectively. These are expressed in terms of the in-plane biaxial strain ε as

$$\Delta E_H = 2a\left(\frac{C_{11} - C_{12}}{C_{11}}\right)\varepsilon, \tag{3}$$

$$\Delta E_S = b\left(\frac{C_{11} + 2C_{12}}{C_{11}}\right)\varepsilon. \tag{4}$$

In these expressions, a (a_c for the conduction band and a_v for the valence band) and b are the hydrostatic and uniaxial deformation potentials, respectively, and C_{ij} are the elastic stiffness constants of GaAs. The strain ε in the GaAs layer is given by

$$\varepsilon = \frac{a_{\mathrm{barrier}} - a_{\mathrm{GaAs}}}{a_{\mathrm{GaAs}}}. \tag{5}$$

Here, a_{barrier} and a_{GaAs} denote in-plane lattice constants of barrier and GaAs, respectively. Under biaxial compressive strain, the degeneracy between the HH and LH valence bands is lifted, resulting in an upward shift of the HH band and a downward shift of the LH band relative to their positions in the unstrained case. Conversely, under tensile strain, the LH band moves upward and the HH band shifts downward.

Due to quantum confinement, the HH and the LH bands experience a downward shift in energy as a result of hole confinement in the quantum well. However, because the LH band has a smaller effective mass than the HH band, it undergoes a larger confinement-induced energy shift. As a result, the LH band shifts downward more significantly than the HH band, introducing a band splitting that is independent of strain effects. This confinement-induced splitting can either complement or counteract the band splitting arising from strain, depending on the nature of the applied strain.

The band splitting due to quantum confinement for each well and barrier material combination was evaluated using the envelope function approximation[37] to solve the Schrödinger equation for electron and hole wavefunctions within the quantum-confined semiconductor superlattice using Schrödinger Equation interface available in COMSOL Multiphysics.[38] The equation was solved in one dimension, using a position-dependent effective mass approximation. The potential profile was constructed from the conduction and valence band offsets between GaAs and $Ga_xIn_{1-x}P$, including strain-induced band edge shifts where applicable. The CBO and VBO were determined using Anderson's rule which provides a first-order approximation based on electron affinities and bandgaps.[30,39–41] Notably, the calculated conduction band offset slightly overestimates experimental values for GaAs/$Ga_xIn_{1-x}P$ heterostructures from scanning tunneling spectroscopy, implying a lower valence band offset and thus a conservative estimate of the

valence band splitting in our model.[42] The effective masses for the conduction band, HH band, and LH band were taken from Refs. 30 and 39. To accurately capture the electronic structure, strain-induced valence band splitting, calculated using Eqs. (1)–(5) was included in the model, allowing for the calculation of the total HH–LH energy separation specific to each superlattice configuration. The Linear Algebra PACKage (LAPACK) based eigenvalue solver implemented in COMSOL computes all eigenstates for the defined finite potential profile, allowing us to accurately capture the confinement-induced band edge shifts. The simulations were performed using periodic boundary conditions to represent a repeating heterostructure. This approach is valid as the number of periods in experimental structures is large enough to render edge effects negligible.

Simulations were performed across a range of well and barrier thicknesses, varying from 2 to 5 nm, to evaluate the influence of layer dimensions on band splitting and confinement effects. The effective masses used for calculation for wells and the barriers are summarized in Table I. The effective masses used in the simulation were assumed to be isotropic. This simplification is commonly adopted in 1D quantum confinement models, particularly for the conduction band where the effective mass is nearly isotropic. For the valence band, although the heavy-hole and light-hole bands are inherently anisotropic, we used direction-specific scalar values along the [100] direction to capture the confinement effects while maintaining computational efficiency. The mixing of electron wavefunctions in adjacent quantum wells leads to energy level splitting and hence the formation of mini-bands instead of discrete energy levels. The first eigenvalue of the mini-bands for each HH and LH band was selected forming the basis for evaluating the HH–LH splitting in each superlattice design as discussed in the following sections.

TABLE I. Material parameters used in the simulation.

Parameter	GaAs	$Ga_xIn_{1-x}P$
m^*_{cb} (in units of m_0)	0.062[30,39]	0.101 (x = 0.65)[30,39] 0.094 (x = 0.51)[30,39] 0.088 (x = 0.39)[30,39]
m^*_{HH} (in units of m_0)	0.350[30,39,43,44]	0.397 (x = 0.65)[30,39] 0.427 (x = 0.51)[30,39] 0.452 (x = 0.39)[30,39]
m^*_{LH} (in units of m_0)	0.090[30,39]	0.172 (x = 0.65)[30,39] 0.160 (x = 0.51)[30,39] 0.151 (x = 0.39)[30,39]
E_g (eV), unstrained	1.424[30,39]	2.135 (x = 0.65)[30,39] 1.917 (x = 0.51)[30,39] 1.751 (x = 0.39)[30,39]
C_{11} (N/m^2)	1.221×10^{11}[30,39]	…
C_{12} (N/m^2)	5.660×10^{10}[30,39]	…
a_c (eV)	−7.1700[30,39]	…
a_v (eV)	−1.1600[30,39]	…
b (eV)	−2.0000[30,39]	…
Δ_0 (eV)	0.341[30,39]	…

III. RESULTS AND DISCUSSION

A. Compressively strained GaAs wells with GaInP barriers

Figures 2(a) and 2(d) present the simulation results for the HH and LH bandgaps as a function of the well and barrier thickness for GaAs/$Ga_{0.65}In_{0.35}P$ superlattice structures. Figure 3(a) depicts the band splitting. The simulation was performed using the envelope function approximation to solve for the electron and hole wavefunctions in the quantum-confined semiconductor system as described in Sec. II. Strain-induced valence band splitting (with 1% compressive strain) was included in the model to accurately compute the total HH–LH separation for each superlattice configuration.

As shown in Fig. 3(a), the band splitting reaches approximately 140 meV for the smallest well thickness (2 nm) combined with the largest barrier thickness (5 nm), while it decreases to about 108 meV for the largest well (5 nm) and smallest barrier (2 nm) configuration—consistent with expectations from quantum confinement theory. Notably, even the smallest band splitting observed exceeds that of the GaAs/$GaAs_{0.65}P_{0.35}$ system when strain effects are included. This enhanced splitting ensures access to a wider energy separation and should lead to higher spin polarization, resulting from a greater density of states in the heavy-hole band. Consequently, this contributes to an increase in QE at elevated ESP, thereby improving the overall figure of merit ($ESP^2 \cdot QE$).

Figure 4(a) illustrates the band alignment of the GaAs/$Ga_{0.65}In_{0.35}P$ heterostructure. For gallium-rich alloys of $Ga_xIn_{1-x}P$ such as $Ga_{0.65}In_{35}P$, approximately 50% of the bandgap difference of $Ga_{0.65}In_{35}P$ with GaAs is attributed to the CBO. Consequently, the conduction band edge of $Ga_{0.65}In_{65}P$ lies about 0.35 eV above, while the valence band edge is positioned approximately 0.35 eV below that of GaAs as represented by CBO and VBO, respectively. Furthermore, due to compressive strain, the conduction band moves up by $\delta_{C,S} \sim 0.07$ eV due to the hydrostatic component of the strain which further reduces the CBO and is comparable to that of the GaAs/$GaAs_{0.65}P_{0.35}$ system. Although the conduction band mass discontinuity factor of 1.63 for the GaAs/$Ga_{0.65}In_{0.35}P$ system is slightly higher than that of the GaAs/$GaAs_{0.65}P_{0.35}$ system (1.30), the enhanced HH–LH band splitting in the GaAs/$Ga_{0.65}In_{0.35}P$ superlattice enables access to higher-energy electrons originating from the heavy-hole band. This should facilitate more efficient electron transport across the barrier layers. This should, in turn, contribute to improved QE from the photocathode, while maintaining high electron spin polarization, thereby improving the overall figure of merit ($ESP^2 \cdot QE$).

B. Lattice-matched GaAs wells with GaInP barriers

Figures 2(b) and 2(e) present the simulation results for the HH and LH bandgaps, while Fig. 3(b) depicts the band splitting as a function of the well and barrier thickness for GaAs/$Ga_{0.51}In_{0.49}P$ superlattice structures.

As shown in Fig. 3(b), the band splitting reaches approximately 75 meV for the smallest well thickness (2 nm) combined with the largest barrier thickness (5 nm). Conversely, the splitting

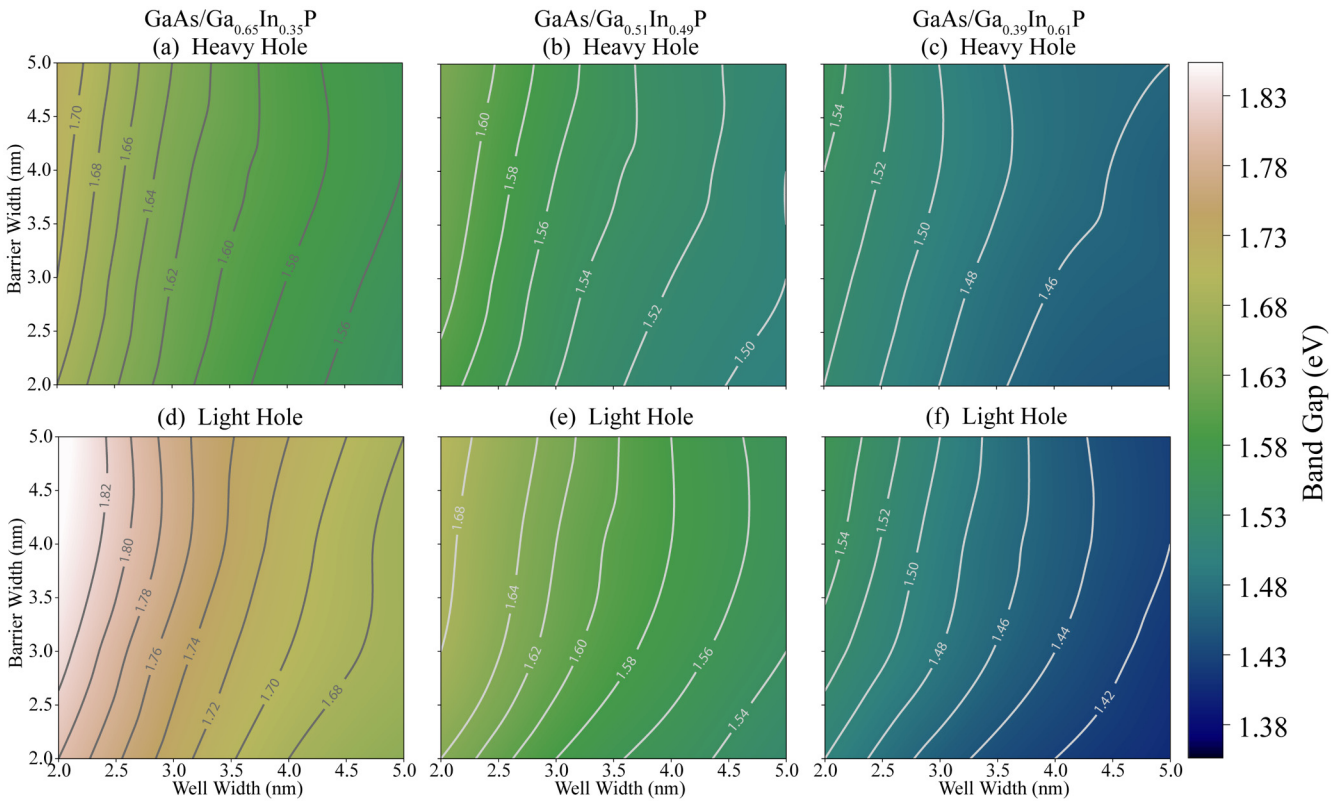

FIG. 2. Heavy-hole (HH) and light-hole (LH) bandgaps incorporating both strain and quantum confinement effects as functions of well and barrier thickness. (a) HH and (d) LH bandgap for a GaAs quantum well with $Ga_{0.65}In_{0.35}P$ barriers, which impose in-plane compressive strain on GaAs. (b) HH and (e) LH bandgap for a GaAs well with lattice-matched $Ga_{0.51}In_{0.49}P$ barriers. (c) HH and (f) LH bandgap for a GaAs well with $Ga_{0.39}In_{0.61}P$ barriers, introducing in-plane tensile strain on GaAs.

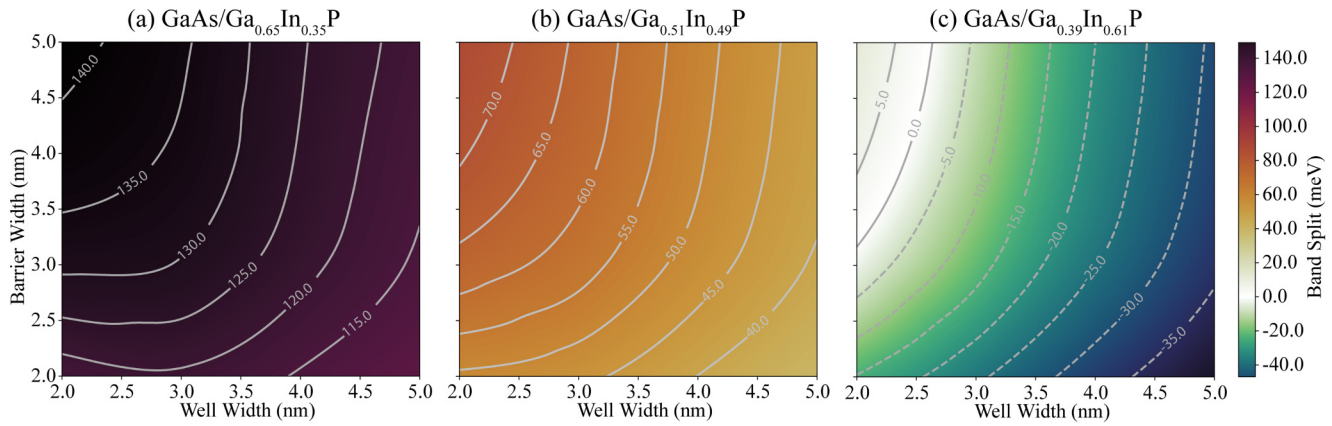

FIG. 3. Band split (heavy-hole to light-hole valence band splitting) as a function of well and barrier thicknesses for (a) Compressively strained GaAs well with $Ga_{0.65}In_{0.35}P$ barriers (b) GaAs well with lattice-matched $Ga_{0.51}In_{0.49}P$ barriers and (c) Tensile strained GaAs well with $Ga_{0.39}In_{0.61}P$ barriers. The solid contour lines show the band splitting when $E_{g,HH} < E_{g,LH}$ whereas the dotted contour lines show the band splitting when $E_{g,HH} > E_{g,LH}$. Here, $E_{g,HH}$ and $E_{g,LH}$ are HH and LH bandgaps after accounting for strain and quantum confinement effects.

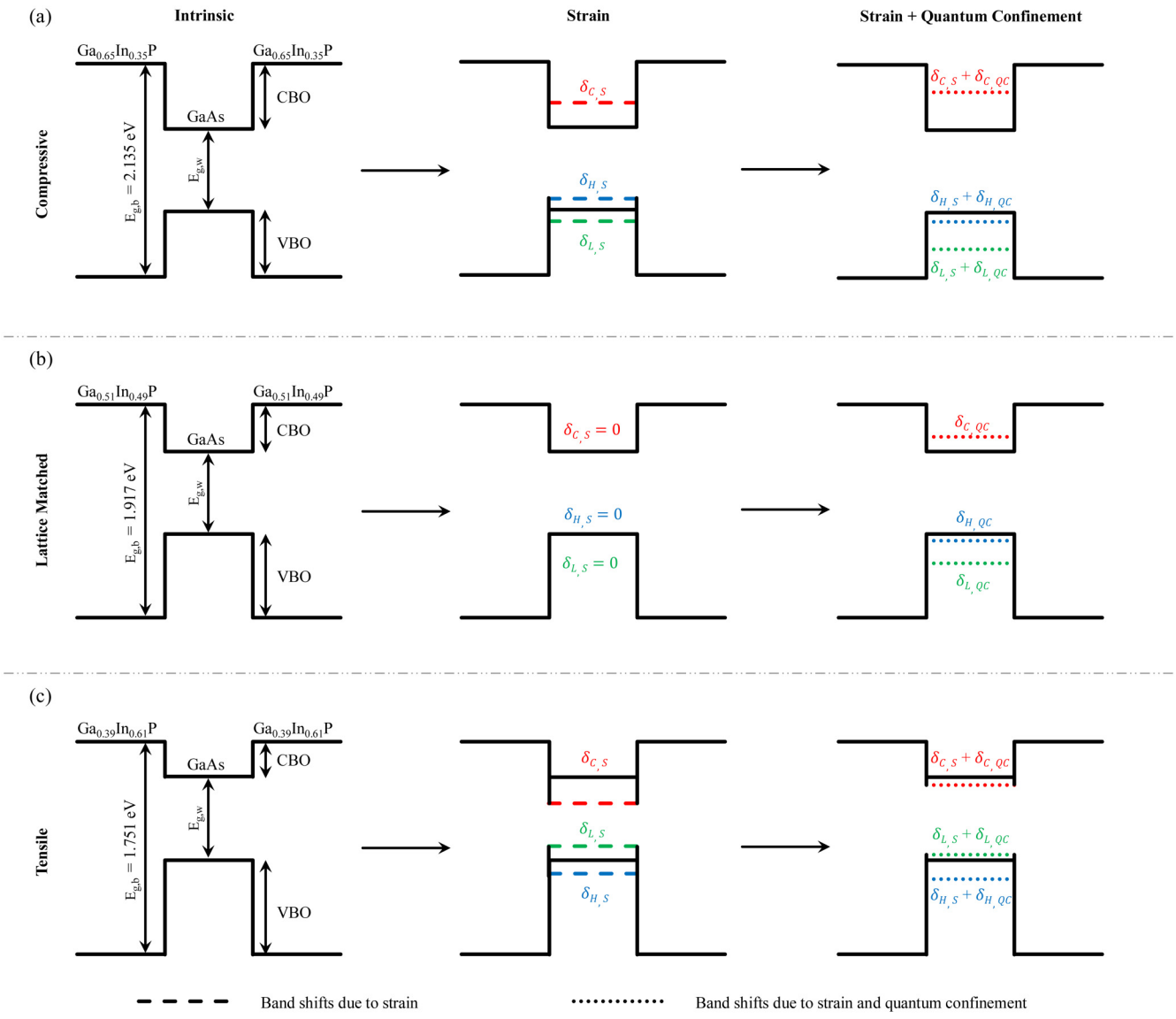

FIG. 4. The band shift due to the effects of strain and quantum confinement. (a) shows the band shifts due to compressive strain (b) the band shifts due to lattice matched and (c) the band shifts due to tensile strain on GaAs well sandwiched between $Ga_xIn_{1-x}P$ barriers. Here, $E_{g,b}$ and $E_{g,w}$ denote the bandgap of bulk barriers and wells, respectively. CBO and VBO represent the conduction band and valence band offsets, respectively. $\delta_{C,S}$, $\delta_{H,S}$ and $\delta_{L,S}$ represent the conduction band, HH band and LH band shifts due to in-plane strain on GaAs, respectively. $\delta_{C,QC}$, $\delta_{H,QC}$ and $\delta_{L,QC}$ represent the conduction band, HH band and LH band shifts due to quantum confinement, respectively.

decreases to about 40 meV for the largest well thickness (5 nm) and smallest barrier thickness (2 nm). In both the cases, the HH band lies above the LH band. Quantum confinement causes both HH and LH bands to shift downward due to carrier localization in the well, with the LH band experiencing a larger shift due to its lower effective mass. The resulting band splitting observed here is comparable to that observed in the compressively strained GaAs/$GaAs_{0.65}P_{0.35}$ system, where strain effects are also included and is comparable or higher than the one observed in GaAs/$Al_{0.35}Ga_{0.65}As$ systems.

For lattice-matched alloy of $Ga_xIn_{1-x}P$ with GaAs, approximately 20%–25% of the bandgap difference with GaAs is attributed to the CBO.[30,39] Consequently, the conduction band edge of $Ga_{0.51}In_{49}P$ lies about 0.18 eV above, that of GaAs with some reports even indicating lower CBO of 0.12 eV,[45] while the valence band edge is positioned approximately 0.31 eV below as

represented by CBO and VBO, respectively, in Figure 4(b). The conduction band mass discontinuity factor for the GaAs/$Ga_{0.51}In_{0.49}P$ system is 1.51. This relatively small mass discontinuity factor, combined with the lower CBO, should facilitate more efficient electron transport across the barrier layers, thereby enhancing the QE of the photocathode.

Additionally, at the point of band splitting, electron emission predominantly occurs from the HH band, which possesses a higher density of states compared to the LH band. This should contribute to an enhancement in the overall QE of the superlattice photocathode. Moreover, the pronounced heavy-hole–light-hole band splitting in the lattice-matched GaAs/$Ga_{0.51}In_{0.49}P$ superlattice structure provides access to higher-energy electrons originating from the HH band, enabling more efficient transport across the barrier layers.

Since this configuration is lattice-matched, a large number of superlattice periods can be grown without introducing significant strain-induced defects, which could otherwise lead to spin-flip scattering and degradation of ESP. These combined advantages should result in improved QE while preserving high ESP.

Another key advantage of the lattice-matched configuration is the elimination of shear strain within the superlattice structure. In non-lattice-matched systems, lattice mismatch induces shear strain components that lead to in-plane asymmetries in the electronic band structure. These asymmetries manifest as anisotropic optical transition probabilities, resulting in QE anisotropy—where the photoemission yield depends on the polarization or orientation of the incident light. By ensuring lattice matching between the well and barrier materials, the shear strain is effectively suppressed, preserving in-plane symmetry and thereby minimizing or eliminating QE anisotropy.

C. Tensile strained GaAs wells with GaInP barriers

Figures 2(c) and 2(f) present the simulation results for the HH and LH bandgaps, while Fig. 3(c) depicts the band splitting as a function of the well and barrier thickness for GaAs/$Ga_{0.39}In_{0.61}P$ superlattice structures. Strain-induced valence band splitting (with 1% tensile strain) was included in the model to accurately compute the total HH–LH separation for each superlattice configuration.

As shown in Fig. 3(c), the band splitting reaches approximately 10 meV for the smallest well thickness (2 nm) combined with the largest barrier thickness (5 nm), with the HH band lying above the LH band. Conversely, the splitting increases to about 40 meV for the largest well thickness (5 nm) and smallest barrier thickness (2 nm), where the LH band lies above the HH band. Under tensile strain, the LH band shifts upward while the HH band moves downward in energy. In contrast, quantum confinement causes both HH and LH bands to shift downward due to carrier localization in the well, with the LH band experiencing a larger shift due to its lower effective mass. Therefore, in tensile-strained, quantum-confined superlattices, the effects of strain and confinement act in opposition with respect to the HH–LH band splitting.

For indium-rich alloys of $Ga_xIn_{1-x}P$ such as $Ga_{0.39}In_{0.61}P$ approximately 13%–18% of the bandgap difference with GaAs is attributed to the CBO.[39] Consequently, the conduction band edge of $Ga_{0.61}In_{39}P$ lies about 0.06 eV above while the valence band edge is positioned approximately 0.27 eV below that of GaAs as represented by CBO and VBO, respectively, in Figure 4(c). Although, due to tensile strain, the conduction band moves down by $\delta_{C,S} \sim 0.07$ eV which increases the CBO, the resulting CBO is still approximately three times smaller than that of the GaAs/$Al_{0.35}Ga_{0.65}As$ system. The conduction band mass discontinuity factor for the GaAs/$Ga_{0.39}In_{0.61}P$ system is 1.42. This relatively small mass discontinuity factor, combined with the lower CBO, should facilitate more efficient electron transport across the barrier layers, thereby enhancing the QE of the photocathode.

It is worth noting that although emission occurs from the LH band—which has a lower density of states compared to the HH band—the use of wider wells should compensate for this by enabling more electrons to be excited across the bandgap, thereby enhancing the overall QE of the superlattice photocathode. Additionally, defects arising from tensile strain are typically oriented parallel to the direction of electron transport and thus exert minimal influence on the spin-flip mechanism for the case of ESP.[28] Together, these effects should potentially allow for simultaneous optimization of QE and ESP, thereby improving the overall figure of merit for spin-polarized electron sources.

IV. CONCLUSION AND FUTURE OUTLOOK

In this study, we have systematically designed and simulated various superlattice configurations to enhance HH–LH band splitting beyond 40 meV, while optimizing band alignment to maximize hole confinement and maintain efficient electron transport. This dual optimization is critical for achieving both high ESP and high QE—key performance metrics for next-generation spin-polarized electron sources.

Three superlattice architectures were investigated: (1) compressively strained GaAs wells on $Ga_{0.65}In_{0.35}P$ barriers, (2) quantum-confined, lattice-matched GaAs/$Ga_{0.51}In_{0.49}P$ structures, and (2) tensile strained GaAs wells on $Ga_{0.39}In_{0.61}P$ barriers. For each configuration, the envelope function approximation was employed to compute the electron and hole wavefunctions under quantum confinement, with strain-induced valence band splitting included in the simulations.

Our work establishes a framework for engineering spin-polarized photocathodes that may enhance the merit by leveraging strain, quantum confinement, and optimized material interfaces. Among the configurations, the compressively strained GaAs/$Ga_{0.65}In_{0.35}P$ superlattice yielded the highest band splitting of approximately 140 meV. The quantum-confined GaAs/$Ga_{0.51}In_{0.49}P$ superlattice achieved up to 75 meV of HH–LH separation, while the tensile strained GaAs/$Ga_{0.39}In_{0.61}P$ system exhibited a maximum splitting of approximately 40 meV. These results demonstrate the tunability of band splitting through careful control of strain and layer dimensions, as well as the importance of proper band alignment to avoid impeding conduction band electron transport. Although maximizing band splitting is desirable for enhancing spin polarization, it is not the sole determinant of a photocathode's figure of merit. The transport properties of electrons through the superlattice, along with the presence of defects within the photocathode structure, play a critical role in its practical performance. Therefore, a more comprehensive theoretical and

computational analysis is essential to quantitatively predict both the QE and ESP. Such analysis is crucial for the rational design and engineering of advanced photocathodes, particularly in preparation for the next generation of high-precision nuclear physics experiments.[10,11,46]

As a next step, we plan to fabricate the proposed superlattice structures using either Molecular Beam Epitaxy (MBE)[47,48] or Metal-Organic Chemical Vapor Deposition (MOCVD),[49] both of which offer the precision necessary for engineering well-defined quantum-confined heterostructures. The fabricated samples will be characterized using a MicroMott polarimeter to experimentally evaluate their ESP and QE.[50] These measurements will serve to validate our simulation results and assess the practical viability of the designs for use in next-generation spin-polarized electron sources. In addition, we also plan to study GaAs/$GaAs_{1-x}P_x$ and GaAs/$Al_xGa_{1-x}As$ superlattice structures. Through this combined theoretical and experimental approach, we aim to advance the development of high-QE, high-ESP photocathodes for accelerator-based applications.

ACKNOWLEDGMENTS

This material was based upon work supported by the U.S. Department of Energy, Office of Science, Office of Nuclear Physics under Contract No. DE-AC05-06OR23177 and Award No. DE-SC0025519.

AUTHOR DECLARATIONS

Conflict of Interest

The authors have no conflicts to disclose.

Author Contributions

A. Kachwala: Conceptualization (equal); Data curation (lead); Formal analysis (lead); Investigation (lead); Methodology (equal); Project administration (supporting); Resources (equal); Software (equal); Validation (lead); Visualization (equal); Writing – original draft (lead); Writing – review & editing (equal). **G. Blume:** Conceptualization (equal); Data curation (supporting); Formal analysis (supporting); Investigation (supporting); Methodology (equal); Project administration (supporting); Resources (equal); Software (equal); Validation (supporting); Visualization (supporting); Writing – review & editing (equal). **S. Marsillac:** Conceptualization (equal); Formal analysis (supporting); Funding acquisition (equal); Investigation (supporting); Methodology (equal); Project administration (supporting); Resources (equal); Software (equal); Supervision (equal); Validation (supporting); Visualization (supporting); Writing – review & editing (equal). **J. Grames:** Conceptualization (equal); Formal analysis (supporting); Funding acquisition (equal); Investigation (supporting); Methodology (equal); Project administration (lead); Resources (equal); Software (equal); Supervision (equal); Validation (supporting); Visualization (supporting); Writing – review & editing (equal). **M. Grau:** Conceptualization (equal); Formal analysis (supporting); Funding acquisition (equal); Investigation (supporting); Methodology (equal); Project administration (supporting); Resources (equal); Software (equal); Validation (supporting); Visualization (equal); Writing – review & editing (equal).

DATA AVAILABILITY

The data that support the findings of this study are available from the corresponding author upon reasonable request.

REFERENCES

[1]A. Subashiev, Y. P. Yashin, J. Clendenin, and Y. A. Mamaev, "Spin polarized electrons: Generation and applications," Phys. Low Dimens. Struct. **1**, 1–36 (1998).
[2]M. Woods, "Polarization at SLAC," AIP Conf. Proc. **343**, 230–244 (1995).
[3]M. Woods, "The polarized electron beam for the SLAC linear collider," arXiv hep-ex/9611006 (1996).
[4]P. Cooper, "Experiments with polarized electron beams at SLAC," in *Antiproton, Polarized Proton, and Polarized Antiproton Beams at Fermilab Energies* (Fermilab, 1977), p. 126.
[5]K. Aulenbacher, C. Nachtigall, H. Andresen, J. Bermuth, T. Dombo, P. Drescher, H. Euteneuer, H. Fischer, D. Harrach, P. Hartmann *et al.*, "The MAMI source of polarized electrons," Nucl. Instrum. Methods Phys. Res., Sect. A **391**, 498–506 (1997).
[6]C. W. Leemann, D. R. Douglas, and G. A. Krafft, "The continuous electron beam accelerator facility: Cebaf at the Jefferson Laboratory," Annu. Rev. Nucl. Part. Sci. **51**, 413–450 (2001).
[7]D. Armstrong, J. Arvieux, R. Asaturyan, T. Averett, S. Bailey, G. Batigne, D. Beck, E. Beise, J. Benesch, L. Bimbot *et al.*, "Strange-quark contributions to parity-violating asymmetries in the forward G0 electron-proton scattering experiment," Phys. Rev. Lett. **95**, 092001 (2005).
[8]D. Androic, D. S. Armstrong, A. Asaturyan, T. Averett, J. Balewski, J. Beaufait, R. Beminiwattha, J. Benesch, F. Benmokhtar, J. Birchall *et al.*, "First determination of the weak charge of the proton," Phys. Rev. Lett. **111**, 141803 (2013).
[9]C. Horowitz, S. J. Pollock, P. A. Souder, and R. Michaels, "Parity violating measurements of neutron densities," Phys. Rev. C **63**, 025501 (2001).
[10]J. Benesch, P. Brindza, R. Carlini, J. Chen, E. Chudakov, S. Covrig, M. Dalton, A. Deur, D. Gaskell, A. Gavalya *et al.*, "The MOLLER experiment: An ultra-precise measurement of the weak mixing angle using Møller scattering," arXiv arXiv:1411.4088 (2014).
[11]F. Willeke and J. Beebe-Wang, "Electron ion collider conceptual design report 2021," Technical Report [Brookhaven National Lab. (BNL), Upton, Thomas Jefferson, 2021].
[12]O. Chubenko, S. Karkare, D. A. Dimitrov, J. K. Bae, L. Cultrera, I. Bazarov, and A. Afanasev, "Monte Carlo modeling of spin-polarized photoemission from p-doped bulk GaAs," J. Appl. Phys. **130**, 063101 (2021).
[13]D. T. Pierce, R. Celotta, G.-C. Wang, W. Unertl, A. Galejs, C. Kuyatt, and S. Mielczarek, "The GaAs spin polarized electron source," Rev. Sci. Instrum. **51**, 478–499 (1980).
[14]M. Erbudak and B. Reihl, "Depolarization of photoelectrons emitted from optically pumped GaAs," Appl. Phys. Lett. **33**, 584 (1978).
[15]R. Mair, R. Prepost, H. Tang, E. Garwin, T. Maruyama, and G. Mulhollan, "Anisotropies in strain and quantum efficiency of strained GaAs grown on GaAsP," Phys. Lett. A **212**, 231–236 (1996).
[16]W. Liu, M. Poelker, X. Peng, S. Zhang, and M. Stutzman, "A comprehensive evaluation of factors that influence the spin polarization of electrons emitted from bulk GaAs photocathodes," J. Appl. Phys. **122**, 035703 (2017).
[17]S. Karkare, D. Dimitrov, W. Schaff, L. Cultrera, A. Bartnik, X. Liu, E. Sawyer, T. Esposito, and I. Bazarov, "Monte Carlo charge transport and photoemission from negative electron affinity GaAs photocathodes," J. Appl. Phys. **113**, 104904 (2013).
[18]S. Karkare, L. Boulet, L. Cultrera, B. Dunham, X. Liu, W. Schaff, and I. Bazarov, "Ultrabright and ultrafast III–V semiconductor photocathodes," Phys. Rev. Lett. **112**, 097601 (2014).

[19]Y. A. Mamaev, A. Subashiev, Y. P. Yashin, H.-J. Drouhin, and G. Lampel, "Energy resolved spin-polarised electron photoemission from strained GaAs/GaAsP heterostructure," Solid State Commun. **114**, 401–405 (2000).
[20]R. Prepost and T. Maruyama, "Advances in polarized electron sources," Annu. Rev. Nucl. Part. Sci. **45**, 41–88 (1995).
[21]T. Saka, T. Kato, T. Nakanishi, S. Okumi, K. Togawa, H. Horinaka, T. Matsuyama, and T. Baba, "Spin-polarized electron sources with GaAs–GaAsP superlattices for surface analyses," Surf. Sci. **454**, 1042–1045 (2000).
[22]T. Nakanishi and S. Nakamura, "Development of polarized electron source of GaAs-AlGaAs superlattice and strained GaAs," in *High Energy Spin Physics*, edited by W. Meyer, E. Steffends, and W. Thiel (Springer, 1991), available at https://doi.org/10.1007/978-3-642-76661-9_7.
[23]T. Omori, Y. Kurihara, T. Nakanishi, H. Aoyagi, T. Baba, T. Furuya, K. Itoga, M. Mizuta, S. Nakamura, Y. Takeuchi, M. Tsubata, and M. Yoshioka, "Large enhancement of polarization observed by extracted electrons from the AlGaAs-GaAs superlattice," Phys. Rev. Lett. **67**, 3294–3297 (1991).
[24]J. W. Matthews and A. E. Blakeslee, "Defects in epitaxial multilayers: I. Misfit dislocations," J. Cryst. Growth **27**, 118–125 (1974).
[25]B. Belfore, A. Masters, D. Poudel, G. Blume, S. Polly, E. Wang, S. M. Hubbard, M. Stutzman, J. M. Grames, M. Poelker, M. Grau, and S. Marsillac, "High figure of merit spin polarized electron sources grown via MOCVD," Appl. Phys. Lett. **123**, 222102 (2023).
[26]T. Maruyama, D.-A. Luh, A. Brachmann, J. Clendenin, E. Garwin, S. Harvey, J. Jiang, R. Kirby, C. Prescott, R. Prepost *et al.*, "Systematic study of polarized electron emission from strained GaAs/GaAsP superlattice photocathodes," Appl. Phys. Lett. **85**, 2640–2642 (2004).
[27]R. M. Stroud, A. T. Hanbicki, Y. D. Park, G. Kioseoglou, A. G. Petukhov, B. T. Jonker, G. Itskos, and A. Petrou, "Reduction of spin injection efficiency by interface defect spin scattering in ZnMnSe/AlGaAs–GaAs spin-polarized light-emitting diodes," Phys. Rev. Lett. **89**, 166602 (2002).
[28]X. Jin, Y. Maeda, T. Saka, M. Tanioku, S. Fuchi, T. Ujihara, Y. Takeda, N. Yamamoto, Y. Nakagawa, A. Mano *et al.*, "Highly spin-polarized electron photocathode based on GaAs–GaAsP superlattice grown on mosaic-structured buffer layer," J. Cryst. Growth **310**, 5039–5043 (2008).
[29]T. Forchhammer, E. Veje, and P. Tidemand-Petersson, "Experimental determination of the conduction-band offset at GaAs/$Ga_{1-x}Al_x$ as heterojunctions with the use of ballistic electrons," Phys. Rev. B **52**, 14693–14698 (1995).
[30]S. Maddox, see https://github.com/scott-maddox/openbandparams for "Openbandparams" (accessed July 10, 2025).
[31]J. Gain, M. D. Sarkar, and S. Kundu, "Energy and effective mass dependence of electron tunnelling through multiple quantum barriers in different heterostructures," arXiv arXiv:1002.1931 (2010).
[32]T. Nishitani, T. Nakanishi, M. Yamamoto, S. Okumi, F. Furuta, M. Miyamoto, M. Kuwahara, N. Yamamoto, K. Naniwa, O. Watanabe *et al.*, "Highly polarized electrons from GaAs–GaAsP and InGaAs–AlGaAs strained-layer superlattice photocathodes," J. Appl. Phys. **97**, 094907 (2005).
[33]V. Sankaran and J. Singh, "Tunneling and subband levels in GaAs quantum well with direct and indirect Al_xGa_{1-x} as barriers," Appl. Phys. Lett. **59**, 1963–1965 (1991).
[34]P. M. Solomon, S. L. Wright, and C. Lanza, "Perpendicular transport across (Al, Ga) As and the γ to x transition," Superlattices Microstruct. **2**, 521–525 (1986).
[35]P. J. Saez, *Polarization and Charge Limit Studies of Strained GaAs Photocathodes* (Stanford University, 1997).
[36]S. Pan, H. Shen, Z. Hang, F. H. Pollak, W. Zhuang, Q. Xu, A. Roth, R. Masut, C. Lacelle, and D. Morris, "Photoreflectance study of narrow-well strained-layer In_xGa_1-xAs/GaAs coupled multiple-quantum-well structures," Phys. Rev. B **38**, 3375 (1988).
[37]P. Harrison and A. Valavanis, *Quantum Wells, Wires and Dots: Theoretical and Computational Physics of Semiconductor Nanostructures* (John Wiley & Sons, 2016).
[38]*COMSOL multiphysics reference manual*, version 6.2, COMSOL, Inc., Burlington, MA, 2024.
[39]I. Vurgaftman, J. R. Meyer, and L. R. Ram-Mohan, "Band parameters for III–V compound semiconductors and their alloys," J. Appl. Phys. **89**, 5815–5875 (2001).
[40]J. Chen, "Band engineering of advanced materials for semiconductor devices," Ph.D. thesis (University of Cambridge, 2023).
[41]R. Anderson, "Germanium-gallium arsenide heterojunctions," IBM J. Res. Dev. **4**, 283–287 (1960).
[42]Y. Dong, R. M. Feenstra, M. Semtsiv, and W. Masselink, "Band offsets of InGaP/GaAs heterojunctions by scanning tunneling spectroscopy," J. Appl. Phys. **103**, 073704 (2008).
[43]R. Miller, D. Kleinman, and A. Gossard, "Energy-gap discontinuities and effective masses for GaAs-Al_xGa_1-x as quantum wells," Phys. Rev. B **29**, 7085 (1984).
[44]S. Haldar, V. Dixit, G. Vashisht, S. K. Khamari, S. Porwal, T. Sharma, and S. Oak, "Effect of carrier confinement on effective mass of excitons and estimation of ultralow disorder in Al_xGa_1-xAs/GaAs quantum wells by magneto-photoluminescence," Sci. Rep. **7**, 4905 (2017).
[45]X. Jin, M. Yamamoto, T. Miyajima, Y. Honda, T. Uchiyama, M. Tabuchi, and Y. Takeda, "Mean transverse energy and response time measurements of GaInP based photocathodes," J. Appl. Phys. **116**, 064501 (2014).
[46]G. E. Dodge, "The U.S. nuclear science long range plan," Nucl. Phys. News **34**, 3–4 (2024).
[47]M. Stutzman, A. Engel, and C. Palmstrøm, "Strained superlattice photocathode development using CBE and MBE," Technical Report [Thomas Jefferson National Accelerator Facility (TJNAF), Newport News, 2023].
[48]M. L. Stutzman, A. Engel, Y. Wu, and C. Palmstrøm, "High polarization InAlGaAs/AlGaAs photocathodes grown using MBE," in *20th International Workshop on Polarized Sources, Targets, and Polarimetry (PSTP2024), Jefferson Lab, Newport News, VA, 22–27 September 2024* (SISSA Medialab, 2024).
[49]G. Blume, A. Masters, J. Grames, M. Stutzman, M. Grau, and S. Marsillac, "Preparation of MOCVD-grown photocathodes containing a strained GaAs/GaAsP superlattice," in *Proceedings of the 20th International Workshop on Polarized Sources, Targets, and Polarimetry (PSTP2024)* (SISSA Medialab, 2024).
[50]J. L. McCarter, M. L. Stutzman, K. W. Trantham, T. G. Anderson, A. M. Cook, and T. J. Gay, "A low-voltage retarding-field Mott polarimeter for photocathode characterization," Nucl. Instrum. Methods Phys. Res., Sect. A **618**, 30–36 (2010).